Large-eddy simulation of turbulent confined coannular jets

By KNUT AKSELVOLL and PARVIZ MOIN

Department of Mechanical Engineering, Stanford University, CA 94305, USA

Large-eddy simulation (LES) was used to study mixing of turbulent, coannular jets discharging into a sudden expansion. This geometry resembles that of a coaxial jet-combustor, and the goal of the calculation was to gain some insight into the phenomena leading to lean blow-out (LBO) in such combustion devices. This is a first step in a series of calculations, where the focus is on the fluid dynamical aspects of the mixing process in the combustion chamber. The effects of swirl, chemical reactions and heat release were not taken into account. Mixing of fuel and oxidizer was studied by tracking a passive scalar introduced in the central jet. The dynamic subgrid-scale (DM) model was used to model both the subgrid-scale stresses and the subgrid-scale scalar flux. The Reynolds number was 38000, based on the bulk velocity and diameter of the combustion chamber. Mean velocities and Reynolds stresses are in good agreement with experimental data. Animated results clearly show that intermittent pockets of fuel-rich fluid (from the central jet) are able to cross the annular jet, virtually undiluted, into the recirculation zone. Most of the fuel-rich fluid is, however, entrained into the recirculation zone near the instantaneous reattachment point. Fuel trapped in the recirculation zone is, for the most part, entrained back into the step shear layer close to the base of the burner.

1. Introduction

A coaxial jet-combustor consists of confined coannular jets that discharge into a sudden expansion. The central pipe normally supplies the fuel and the annular pipe supplies the oxidizer (air). This geometry provides a recirculation zone that is similar to those found in modern gas turbine combustors. The recirculation zone established by the step is important because it aids in stabilizing the flame. Figure 1 shows a side-view of the combustor which includes some of the important flow and combustion zones in the device.

When operated in a fuel-rich mode the flame is very stable and is anchored in the jet shear layer by a pilot flame attached to the step near the outer edge of the annular air tube. As the fuel to air ratio decreases, the flame becomes more and more unstable until the point where the entire flame lifts from the base region of the burner and stabilizes further downstream. Reducing the fuel to air ratio even further results in a progressively less stable flame which eventually blows out. This process is known as lean blow-out (LBO).

A precise understanding of the phenomena leading to LBO have become more important recently because advancements in gas turbine technology have reduced design tolerances. The ability to accurately predict LBO for combustion chambers
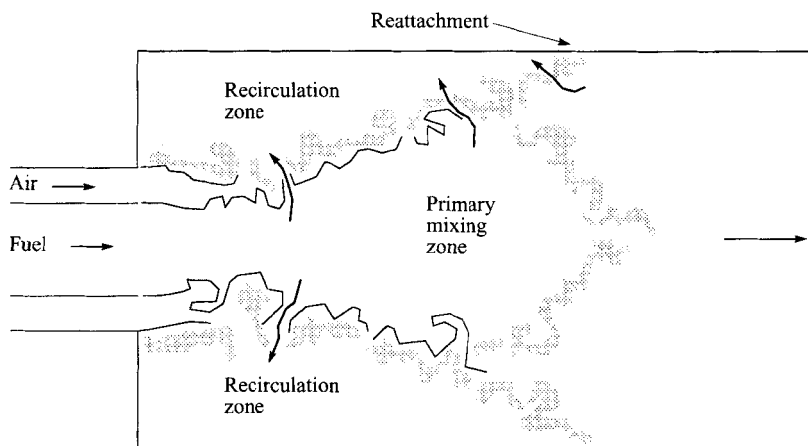
FIGURE 1. Coaxial jet-combustor.

is considered important since it is related to combustion stability which is critical to safety and reliability. The problems related to predicting LBO are many. LBO is usually encountered during engine transients and it may therefore be difficult to separate overall system behavior from the combustor characteristics. The mechanisms of blow-out in one combustor design might therefore be different from those of another design, and even be sensitive to small design changes to the point that manufacturing and assembly tolerances in a system component may be significant factors.

Roquemore et al. (1991) investigated the phenomena related to LBO in a combined experimental and computational study. They observed that there was a certain degree of intermittency associated with the attached and lifted flames such that in the fuel-rich mode the flame would occasionally lift from the base of the burner, but stay attached most of the time. Likewise, in the fuel-lean mode, the flame would occasionally flash back and momentarily attach to the base of the burner, but stay lifted most of the time. Whether the flame is attached or lifted is believed to be closely related to the amount of fuel and hot combustion products being entrained into the recirculation zone.

When running in a fuel-rich mode a region of intense combustion is established in the region where the shear layers between the air and recirculation zone and the air and fuel stream merge (a few central-pipe diameters downstream of the base of the burner). This combustion zone is being fed directly by fuel coming from the fuel jet. However, this flame is piloted by a weaker flame fed from the the recirculation zone and attached at the outer region of the air tube, at the base of the burner. It is proposed that unburned fuel and hot combustion products escape through 'holes' in the flame into the recirculation zone (as indicated by the arrows in figure 1). The holes appear to be formed in the braid regions of the vortex trains. Stretching and fast mixing normally occur in the braid regions which might lead to quenching of the flame by finite rate chemistry, thus forming holes in the flame. However, the formation of holes, and consequent escape of fuel and hot combustion products is a highly intermittent process. The fuel concentration in the recirculation zone might therefore at some points in time be too low to support the pilot flame at the base of the burner and the flame therefore intermittently lifts off. However, the likelihood of this occurring decreases with increasing fuel to air ratio. But as the fuel to air ratio

decreases lift-off becomes more frequent to the point where the flame is lifted most of the time.

The present work uses LES to study the mixing process downstream of the expansion, focusing on the fluid dynamical aspects of the process. Swirl which is usually used to stabilize the flame in real combustors has not been taken into account. Furthermore, all calculations are for cold flows, that is the effects of chemical reactions and heat release have not been accounted for. In order to properly investigate the LBO phenomenon in real combustors both these effects have to be taken into account. The present calculation must therefore be viewed as a first step in this process. The basic fluid dynamical aspects of the mixing process have to be accurately predicted before adding other complicating factors in the calculation. The next step, which involves studying the effect of swirl, is currently under way. There are also plans to include the effects of chemical reactions and heat release.

The calculations performed in this study are designed to match an experimental setup used by Johnson & Bennett (1981, 1984). The experiment used water for both the central and annular jets. The central jet was visualized using dye. The mass flow rate corresponds to a fuel-rich equivalence ratio, which is not necessarily ideal for studying LBO which is characterized by lean fuel conditions. However, since the data base is well documented it is suited as a reference for the present calculations. When the effects of chemical reactions and heat release are included it becomes more important to use a low equivalence ratio in the calculations.

The Reynolds number was 38000, based on the bulk velocity and diameter of the combustion chamber. The velocity ratio of the annular and central jets was 3:1.

2. Governing equations

2.1. *Flow equations*

The governing equations are the filtered Navier–Stokes and continuity equations in cylindrical coordinates. (Filtering is denoted with a bar over the symbols.) The equations are non-dimensionalized using the bulk velocity, U_c, in the central pipe, and the step height, h. (See figure 2 for notation.) They are

$$\frac{\partial \bar{\boldsymbol{u}}}{\partial t} + \nabla \cdot (\bar{\boldsymbol{u}} \otimes \bar{\boldsymbol{u}}) = -\nabla \phi + \nabla \cdot \left\{ v \nabla \bar{\boldsymbol{u}} \right\} + \nabla \cdot \left\{ v (\nabla \bar{\boldsymbol{u}})^T, \right\} \tag{2.1}$$

$$\nabla \cdot \bar{\boldsymbol{u}} = 0, \tag{2.2}$$

where v represents the total viscosity, equal to $v_t + 1/Re$, and v_t is the eddy viscosity. Re is the Reynolds number, $\boldsymbol{u}$ is the velocity vector, and ϕ is the sum of the filtered pressure and the trace of the subgrid-scale stress tensor τ_{ij}, i.e. $\phi = \bar{p} + \frac{1}{3}\tau_{kk}$. The dynamic subgrid-scale (DM) model (Germano *et al.* 1991) with

$$q_{ij} = -2v_t \bar{S}_{ij} \tag{2.3}$$

has been implemented in (2.1) (q_{ij} is the anisotropic part of the subgrid-scale stress tensor, τ_{ij}). The eddy viscosity is calculated according to

$$\left. \begin{array}{ll} v_t = C\bar{\Delta}^2 |\bar{S}|, & C\bar{\Delta}^2 = -\frac{1}{2}\frac{\langle \mathcal{L}_{ij}M_{ij}\rangle_\theta}{\langle M_{ij}M_{ij}\rangle_\theta}, \qquad |\bar{S}| = (2\bar{S}_{ij}\bar{S}_{ij})^{1/2}, \\ \\ \mathcal{L}_{ij} = \widehat{\bar{u}_i \bar{u}_j} - \hat{\bar{u}}_i \hat{\bar{u}}_j, & M_{ij} = \left(\hat{\bar{\Delta}}^2/\bar{\Delta}^2 \right) |\bar{S}| \bar{S}_{ij} - \widehat{|\bar{S}| \bar{S}_{ij}}, \end{array} \right\} \tag{2.4}$$

where $\overline{S}_{ij}$ is the large-scale strain rate tensor, and $\overline{\Delta}$ and $\widehat{\Delta}$ are the filter widths at the grid filter and test filter levels, respectively. $\langle\ \rangle_\theta$ indicates an average taken in the azimuthal direction. A hat over the symbols denotes test-filtered quantities. No explicit grid filtering was done. The grid-filter width, $\overline{\Delta}_i$, was assumed to be equal to the grid spacing, Δx_i. The test-filter width was taken to be twice the grid-filter width (streamwise and spanwise). No explicit test filtering was done in the radial direction. The following definitions (Cabot 1991) were used for the filter widths:

$$\overline{\Delta}^2 = \overline{\Delta}_1\overline{\Delta}_3, \qquad\qquad \widehat{\Delta}^2 = \widehat{\Delta}_1\widehat{\Delta}_3, \qquad (2.5)$$

where subscripts 1 and 3 denote the axial and azimuthal directions, respectively. For additional details, see Akselvoll & Moin (1995).

2.2. *Passive scalar transport equation*

A passive scalar, φ, is used to track mixing of the fuel and air jets in the combustion chamber; φ represents the fuel mass-fraction in the mixture with $\varphi = 1$ being pure fuel, and $\varphi = 0$ being pure air. After filtering, the equation governing convection and diffusion of a passive scalar is

$$\frac{\partial\overline{\varphi}}{\partial t} = -\nabla\cdot(\overline{u}\,\overline{\varphi}) + \nabla\cdot(\alpha_m\nabla\overline{\varphi} - q), \qquad (2.6)$$

where α_m is the molecular diffusivity. The equation has been non-dimensionalized using the same variables as used in the governing flow equations. The vector q gives the subgrid-scale scalar flux. It should not be confused with the tensor q_{ij} used to denote the anisotropic part of the subgrid-scale stresses. The subgrid-scale scalar flux represents transport of the scalar φ caused by turbulent scales too small to be resolved on the computational grid. It is given by

$$q = \overline{u\varphi} - \overline{u}\,\overline{\varphi}. \qquad (2.7)$$

Following the approach of Moin *et al.* (1991), the subgrid-scale scalar flux is modelled assuming that it is aligned with the scalar gradient vector:

$$q = -\alpha_t\nabla\overline{\varphi}, \qquad \alpha_t = Sc_t/\nu_t, \qquad (2.8)$$

where α_t is the eddy diffusivity, and Sc_t is the subgrid-scale turbulent Schmidt number. The eddy diffusivity is determined following the procedures of the dynamic subgrid-scale model (see Moin *et al.* 1991 for details).

3. Numerical method

3.1. *Computational domain and flow rates*

The computational domain is shown in figure 2. A length scale is provided by the step height, h, and a velocity scale is provided by the bulk velocity in the central pipe, U_c. All variables are non-dimensionalized using h and U_c. The bulk velocity in the annular pipe is U_a, and U_0 is the bulk velocity in the combustion chamber. The wall between the central pipe and the annular pipe is assumed to be infinitely thin. The coordinate system is located at the point of expansion, with $r = 0$ at the centreline; x is used to denote the axial (or streamwise) coordinate, and θ is used to denote the azimuthal coordinate. The radial dimensions are the same as those in the experimental facility of Johnson & Bennett (1981, 1984). Note that the radius of the central pipe corresponds to the radius at the end of the tapered section of the central pipe in the experimental facility (see figure 4 for details of the experimental facility).
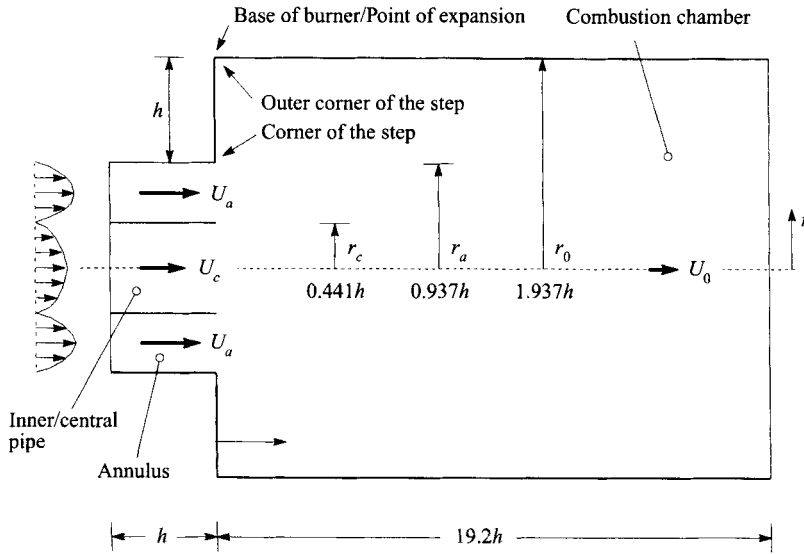
FIGURE 2. Computational domain for the coaxial jet-combustor.

	Central	Annular	Comb. chamber
U_{bulk}/U_c calc.	1.0	3.132	0.600
U_{bulk}/U_c exp.	1.0	3.192	0.612
$Q/(h^2 U_c)$ calc.	0.741	6.308	7.049
$Q/(h^2 U_c)$ exp.	0.758	6.456	7.214

TABLE 1. Bulk velocities and volumetric flow rates used in the calculation (calc.) and the experiment (exp.) (Johnson & Bennet).

Table 1 gives the volumetric flow rates for the simulation as well as the flow rates used by Johnson & Bennett. The Reynolds number, based on the step height, h, and the bulk velocity in the central pipe, U_c, was 16400.

3.2. *Computational grid*

The governing equations are discretized in space using a second-order finite volume formulation. The calculation used $215 \times 76 \times 128$ grid points in the axial, radial, and azimuthal directions, respectively. 34 of the 215 axial grid points were used to cover the inlet section (upstream of the expansion). This resolution was shown to yield grid-independent results (see Akselvoll & Moin 1995). The axial grid is compressed around the point of expansion and stretched on either side. The radial grid is stretched in order to cluster grid points along all solid walls, both upstream and downstream of the expansion.

3.3. *Boundary conditions*

No-slip boundary conditions are used along all solid walls. Periodic condition is applied in the azimuthal direction. The convective boundary condition:

$$\frac{\partial u_i}{\partial t} + U_{con}\frac{\partial u_i}{\partial x} = 0, \tag{3.1}$$

was applied at the exit of the domain. The convective velocity, U_{con}, is set equal to the mean axial velocity integrated across the exit plane. Akselvoll & Moin (1995) found, by comparing the solutions from calculations with two different axial lengths, that this condition had no visible effect on the flow statistics up to about $1h$ upstream of the exit boundary. Similar but more extensive tests were performed by Le & Moin (1994) who applied the convective outflow condition in a direct numerical simulation of turbulent flow over a backward facing step. Their conclusion was the same regarding the zone of influence of the outflow boundary condition.

The inflow boundary condition consists of velocity planes extracted from a separate unsteady three-dimensional calculation of a turbulent coaxial pipe flow, with radial dimensions identical to those of the inlet section of the coaxial jet-combustor. The radial and azimuthal grids used in the periodic pipe-flow section are identical to those in the inlet section of the coaxial jet-combustor. The axial grid is uniform with spacing equal to the axial grid spacing at the inlet of the computational domain of the coaxial jet-combustor. The boundary condition prescribed at the inlet of the coaxial jet-combustor is therefore independent of the flow in the combustor. Tests were performed varying the length of the inlet section of the combustor from h to $5h$ without noticeable effects on the statistical results downstream of the expansion.

For the passive scalar transport equation, periodic boundary condition is used in the azimuthal direction. The outflow boundary condition is the same convective condition as used for the momentum equations. The Neumann condition (gradient of the scalar normal to a surface is zero) is enforced along all horizontal and vertical walls. The inflow boundary condition is determined using a Dirichlet condition: the scalar is set to 1 in the central pipe, and 0 in the annular pipe.

3.4. Temporal integration

A modified third-order Runge–Kutta scheme (Spalart 1987; Spalart, Moser & Rogers 1991) is used for terms treated explicitly and second-order Crank–Nicolson is used for the terms treated implicitly. The fractional step method is used to remove the implicit pressure dependence in the momentum equations.

The special computational problems that arise with cylindrical coordinates can be illustrated by examining the computational grid, displayed in figure 3. The grid is stretched in the radial direction in order to resolve the boundary layers along all walls, including the walls of the central and annular pipes of the inlet section. The fine radial grid which is necessary to resolve the boundary layers in the inlet section extends downstream into the combustion chamber. Since large radial velocities are expected in this region, it is desirable to treat all convective terms with derivatives in the radial direction implicitly. Diffusive terms with derivatives in the radial direction will also have to be treated implicitly. However, in order to get acceptable azimuthal resolution at the outer wall, the azimuthal resolution around the centreline becomes unnecessarily fine. Since the azimuthal convection velocity may be significant around the centreline it is clear that all terms (convective and diffusive) with derivatives in the azimuthal direction should be treated implicitly in order to avoid imposing a severe restriction on the time step.

The approach used to integrate the Navier–Stokes equations in the present study is based on what can be viewed as a temporal domain decomposition method. The computational domain is divided into two separate parts; the so-called 'core region' which includes the centreline and extends to a given radius, r_{core}, and the 'outer region' which includes the rest of the domain. The idea is to treat all terms with derivatives in the azimuthal direction implicitly in the core region. All other terms in this region are
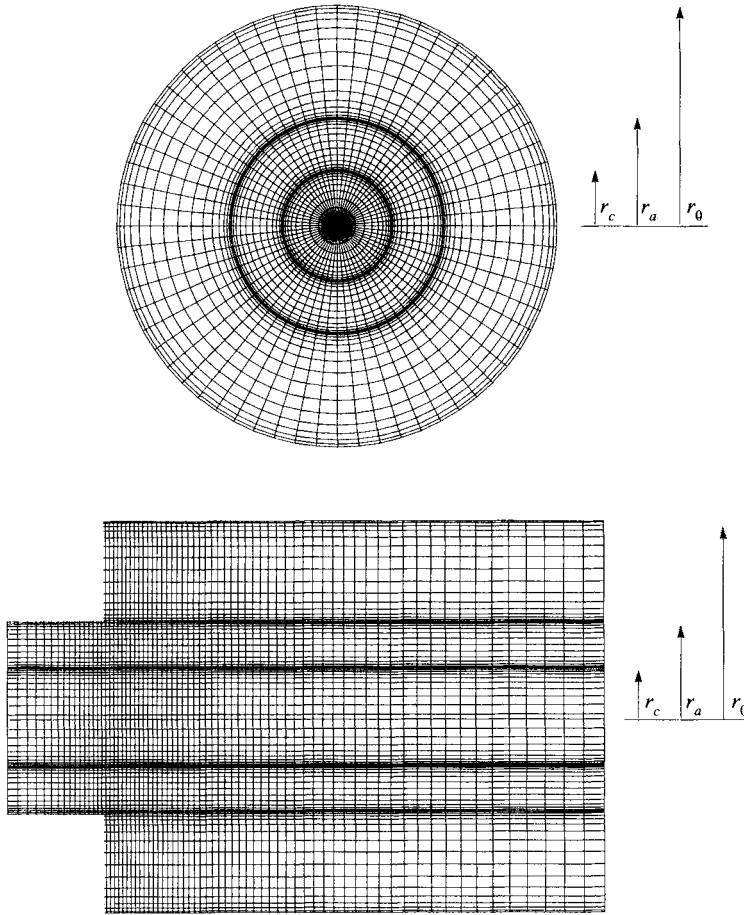
FIGURE 3. Example of computational grid. (This particular grid has fewer points than that used in the calculation, but the distribution of points is similar.)

treated explicitly. In the outer region terms with derivatives in the radial direction are treated implicitly. All other terms are treated explicitly. This procedure simplifies the solution algorithm since only one of the discretized momentum equations is nonlinear in each region.

The interface between the core region and outer region should be located somewhere in the range $0 < r_{core} < r_c$. This assures that all zones with fine radial grid fall in the outer region. The interface itself is treated such that overall second-order temporal accuracy is retained. (Details of this method can be found in Akselvoll & Moin 1995.)

4. Reference case

The present calculation was designed to match as closely as possible the geometry and flow conditions used in an experimental study by Johnson & Bennett (1981, 1984). A sketch of the experimental setup is shown in figure 4. The objective of the experimental study was to obtain data that could be used for evaluation and improvement of turbulent transport models, used for combustor flow modelling. The study used laser velocimeter (LV) and laser-induced fluorescence (LIF) techniques to measure velocities and concentration. Visualization techniques were used to qualita-
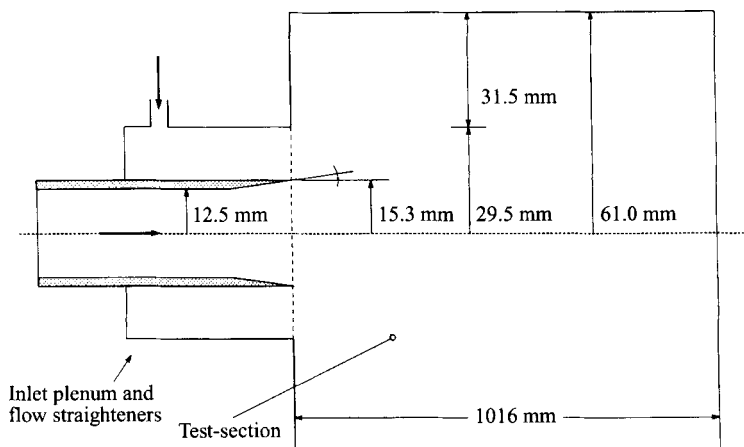
FIGURE 4. Sketch of the experimental setup used by Johnson & Bennett.

tively determine the time-dependent characteristics of the flow as well as the scale and structure of the turbulent eddies.

The inlet plenum for the annular duct contained three perforated plates to produce approximately uniform flow and a honeycomb section to remove swirl from the flow. No flow straightening devices were used for the central pipe which was approximately 25 mm in diameter and was fed through a pipe/hose combination with the same diameter and a total length of over 300 mm.

The main difference between the experimental and the computational geometries is that the central pipe used in the experiment had a fixed-thickness wall with a tapered end. Owing to the structure of the computational code, the calculations were performed assuming an infinitely thin pipe wall of radius 15.3 mm. It was initially thought that this difference would not cause significant discrepancies in the flow characteristics at the point of expansion. However, as the results in the following section indicate, the flow in the experiment may not have been able to adjust to the rather rapid change in diameter, thus causing discrepancies in the inlet conditions between experiment and computation.

Johnson & Bennett made no measurements in either the central or annular pipe in the inlet section thus making a comparison of the flow conditions upstream of the expansion impossible. The section feeding the central pipe of the test facility consisted of a pipe/hose combination of length $24r_c$. It is likely that this was sufficient to ensure fully developed flow in the central pipe, upstream of the tapered section. However, the length of the annular inlet section was not quoted by Johnson & Bennett, and since it contained three perforated plates (at unspecified locations) and a honeycomb section, it is unlikely that the annular flow was fully developed at the point of expansion into the combustion chamber. The calculations were performed assuming fully developed turbulent flow.

5. Results

A comparison of experimental results (Johnson & Bennett) and computational results is presented in §5.1. Section 5.2 focuses on an analysis of the statistical correlations and animated results in order to study the mixing and entrainment processes downstream of the expansion. (A separate, coarser grid calculation was
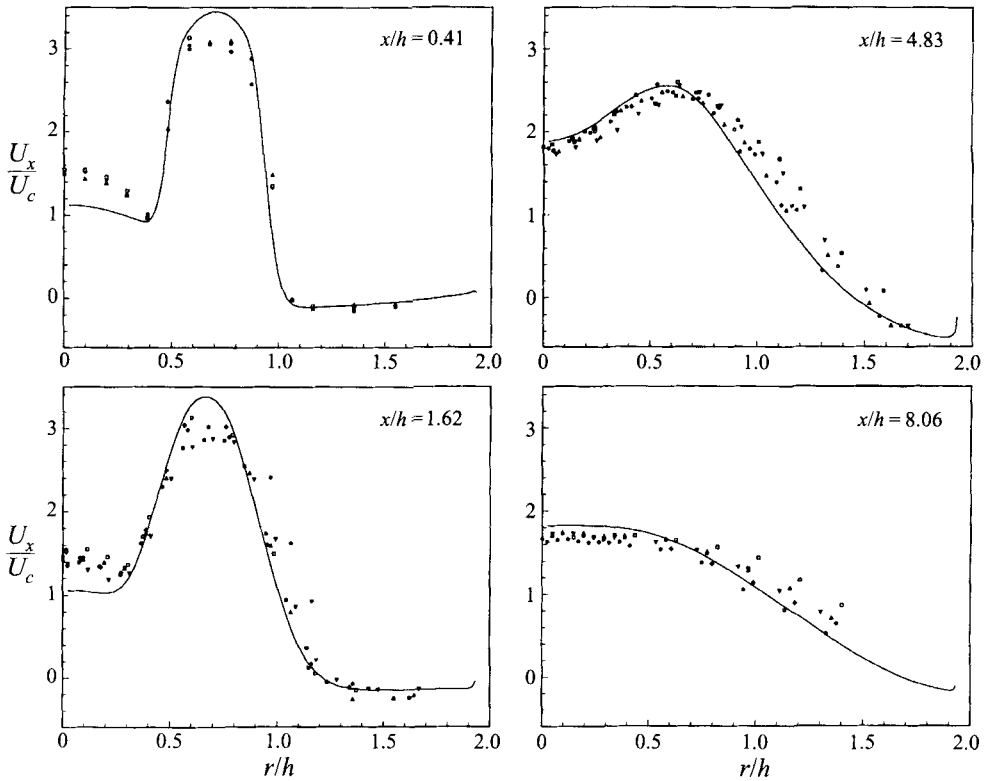
FIGURE 5. Mean axial velocity: ———— , calculation; all symbols, experiment by Johnson & Bennett.

used for the animation. This calculation is described in detail in Akselvoll & Moin 1995.) Note that the central jet is referred to as the fuel jet in the following discussion. Likewise, reference is made to the fuel mass-fraction, which refers to the concentration of central jet fluid in the combustion chamber.

5.1. *Code verification*

Mean axial velocity profiles are shown at four axial measurement stations, ranging from $x/h = 0.41$ to $x/h = 8.06$, in figure 5. Johnson & Bennett made several measurements for the same flow condition. During each run they made measurements at one to four azimuthal locations (at each axial measurement station), spaced $90°$ apart. These measurements are represented by different symbols in the following figures; however, no effort is made to distinguish between measurements taken in different runs or at different azimuthal locations when comparing with the computational results.

The overall agreement between experiment and calculation is seen to be good at most measurement stations. However, closest to the expansion, particularly at $x/h = 0.41$, a fairly significant difference is observed. It seems as though the flow rate in the central jet was higher in the experiment than in the calculation and the converse in the annular air jet.

The reason for the discrepancy can most likely be attributed to the difference in the geometry of the central pipe, described in §4. Tapering of the central pipe in the experiment increases the area of the pipe by 50% within a distance of roughly
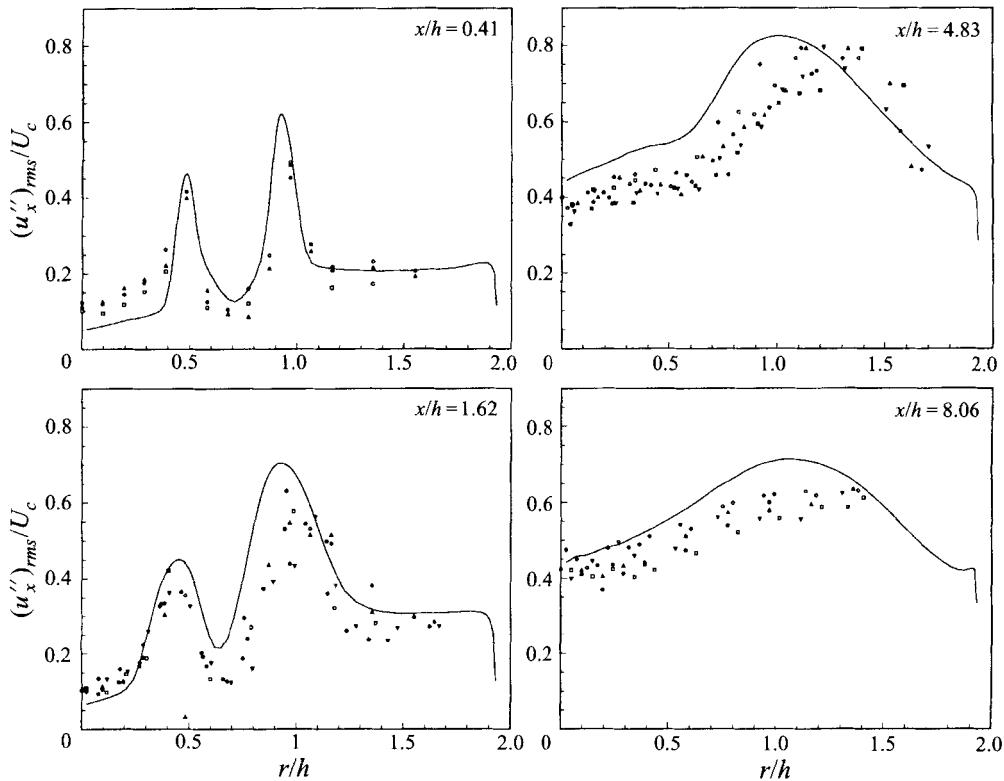
FIGURE 6. Resolved axial turbulence intensity: ——— , calculation;
all symbols, experiment by Johnson & Bennett.

0.7 times the outer diameter of the central pipe. It seems likely that the flow going through the expansion is not fully developed (compared with pipe flow), thus causing only a modest reduction in the centreline velocity. This would explain why the ratio of the peak velocities (located at the centre of the annular and central pipes) is only about 2 in the experiment and about 3 in the calculation (measured at $x/h = 0.41h$). It seems clear that the assumption that the experimental flow is able to adjust through the tapering of the central pipe does not hold. (This was confirmed from a simple Reynolds-averaged calculation which included the tapered end of the central pipe.) Experimental and computational results are therefore likely to be different close to the expansion due to differences in the inflow conditions. However, the effect of different inflow conditions is limited to a short region downstream of the expansion point. The difference between experiment and calculation is still present at $x/h = 1.62$, but has vanished at $x/h = 4.83$. Further downstream only minor differences are observed. In particular it is seen that the calculated velocity profiles lead those of the experiment in the central region of the flow, and lag in the outer part (i.e. for r/h larger than about 0.7).

Figure 6 shows the axial turbulence intensity, $(u_x'')_{rms}$. (Note that LES only gives the resolved part of the turbulence intensities.) Although the qualitative agreement between experimental and computational results is good, the calculation tends to over-predict $(u_x'')_{rms}$ at almost all axial stations. It should also be noticed that there is a rather significant scatter in the experimental data. The tendency to over-predict $(u_x'')_{rms}$ might be related to lack of grid resolution, particularly in the annular pipe in
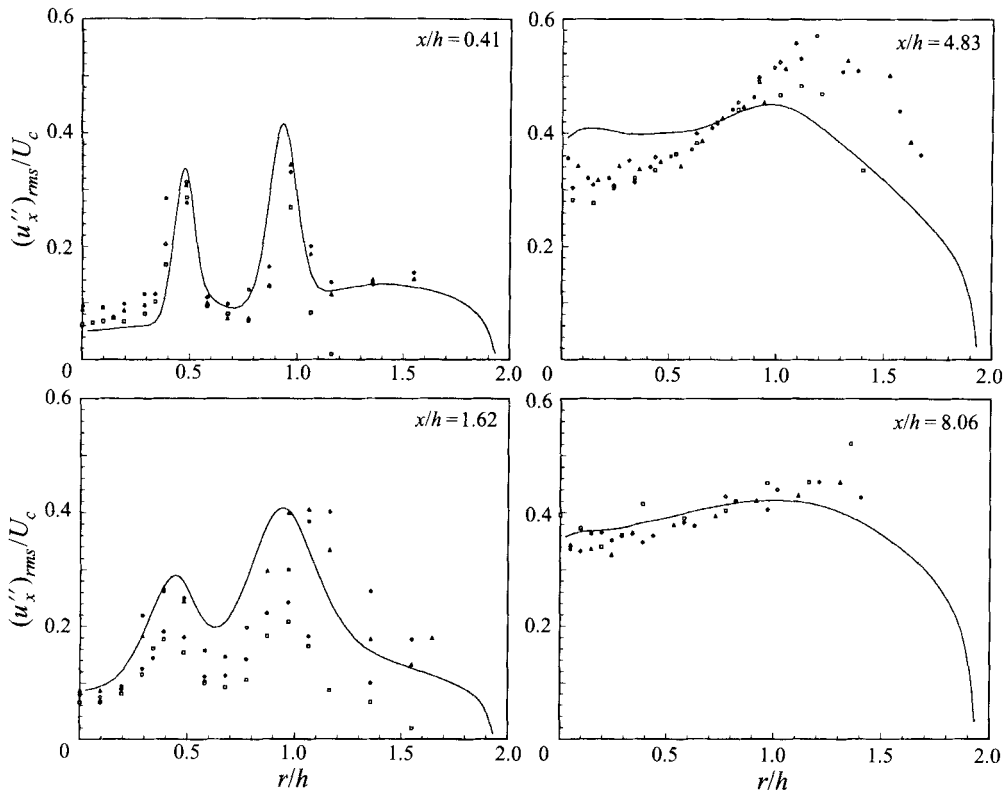
FIGURE 7. Resolved radial turbulence intensity: ——— , calculation; all symbols, experiment by Johnson & Bennett.

the inlet section. It is well known from LES of turbulent channel flow that $(u''_x)_{rms}$ is over-predicted if the spanwise grid resolution is too coarse.

The agreement between experimental and computational results is seen to be better for the radial turbulence intensity, shown in figure 7. As with other quantities there is a significant scatter in the experimental data. At $x/h = 4.83$ the calculation over-predicts $(u''_r)_{rms}$ in the central region and under-predicts $(u''_r)_{rms}$ in the outer part of the flow, compared with the experiment. Despite these differences the qualitative agreement between experiment and calculation is still quite good.

Figure 8 shows the mean concentration profile (fuel mass-fraction). At the first two stations excellent agreement between experimental and calculated results is observed. At $x/h = 4.83$ the agreement remains good between $r/h = 0.4$ and the outer wall; however, the calculation under-predicts the concentration in the core region of the flow. Further downstream the agreement between experiment and computation improves.

5.2. Flow analysis

This section focuses on an analysis of the statistically averaged as well as the animated results, in order to address the issues of mixing and fuel entrainment into the recirculation zone.

Mean flow field characteristics are presented in §5.2.1 and are used to evaluate the flow field and entrainment characteristics of the recirculation zone. Section 5.2.2 presents the instantaneous pressure and passive scalar fields for visualization
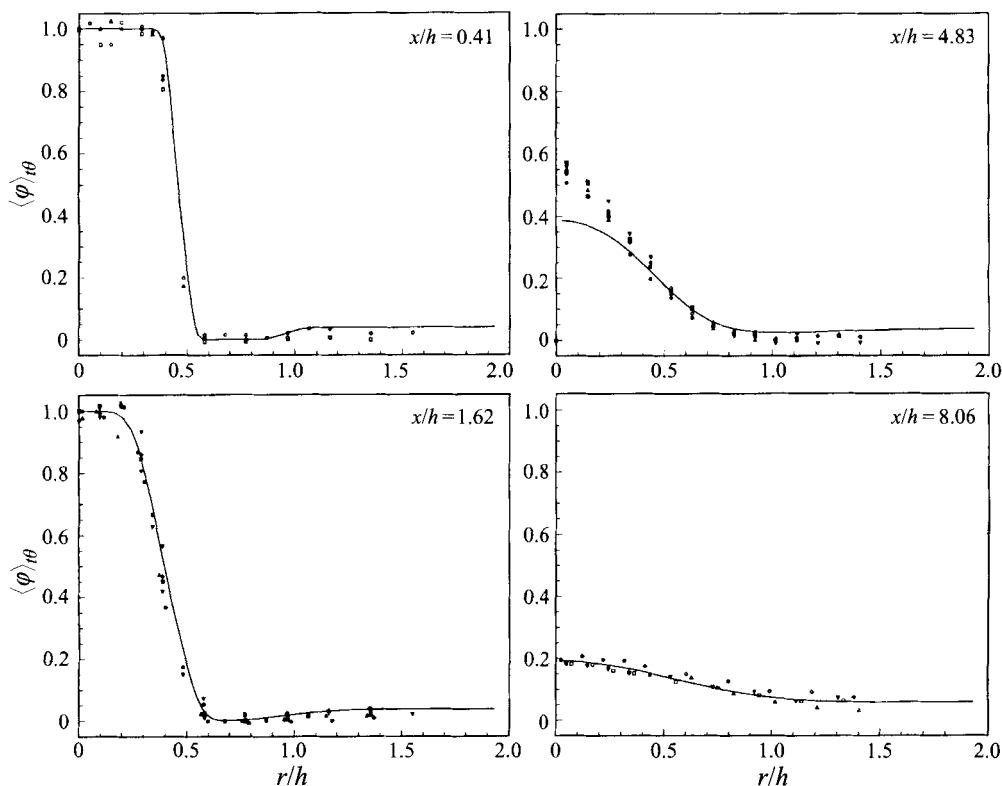
FIGURE 8. Mean value of passive scalar: ———— , calculation; all symbols, experiment by
Johnson & Bennett.

of important large-scale structures. Section 5.2.3 offers an analysis of the fuel mass-fraction distribution in the combustion chamber. This is combined with a description of animated results which sheds some light on instantaneous characteristics of the mixing and entrainment processes.

5.2.1. Analysis of the mean flow field

The reattachment location, defined as the point where the wall-normal gradient of the axial velocity (at the wall) changes sign, is found to be $X_R/h = 9.4$. A second reattachment point is found at $x/h = 1.0$, indicating that there is a secondary, counter-rotating, vortex located in the outer corner of the step. This is confirmed in figure 9 which shows a contour map of the axial and radial velocity components.

Figure 9(a) shows the mean axial velocity. Notice that the contour lines are only shown up to $U_x/U_c = 2.5$. The mean axial velocity ranges from about -0.47 to a maximum of 3.46, with the maximum being located at the centre of the the annular pipe. The largest negative velocity is found close to the wall in the recirculation zone.

Figure 10, shows an enlarged contour map of the region of negative mean axial velocity. It is apparent that the largest backflow occurs very close to the wall. This was also confirmed by the animated results. The animation sequence, showing a contour map of the fuel mass-fraction, showed fuel-rich fluid intermittently moving towards the base of the burner in what seems to be a narrow 'belt', very close to the wall. (Figure 19, described in §5.2.3, provides a graphical illustration of this point.) It

(a)

> 2.5

> 2.5

0   2   4   6   8   10   12   14   16   18

(b)

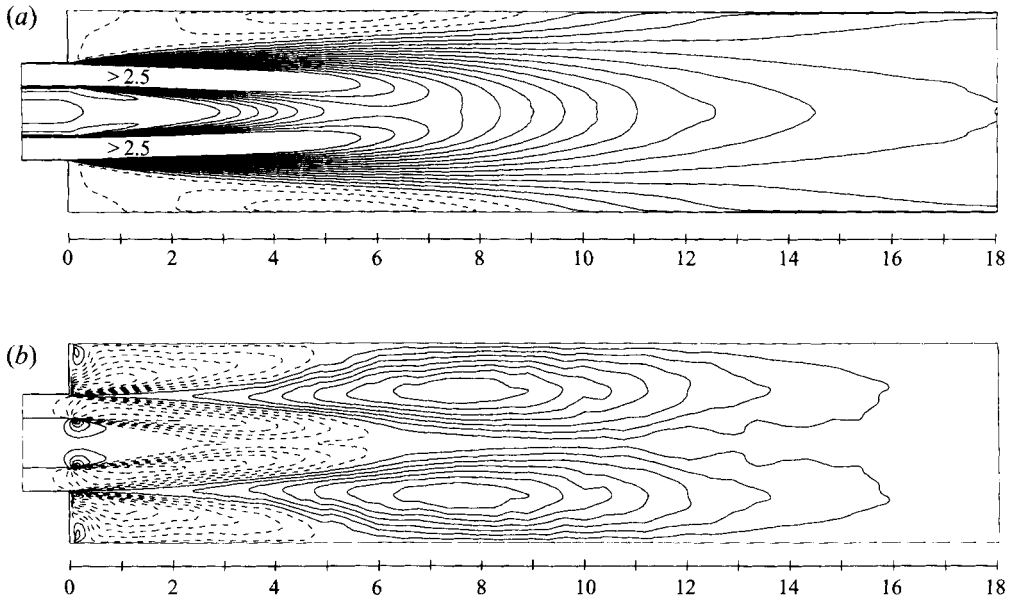0   2   4   6   8   10   12   14   16   18

FIGURE 9. Contour plots of the mean velocity components. Dashed lines denote negative values, solid lines denote positive values. (a) Axial velocity, U_x/U_c. Range : −0.47 to 3.46. Contour levels shown between −0.5 and 2.5 at intervals of 0.15. (b) Radial velocity, U_r/U_c. Range : −0.17 to 0.12. Contour levels shown between −0.17 and 0.12 at intervals of 0.0145.
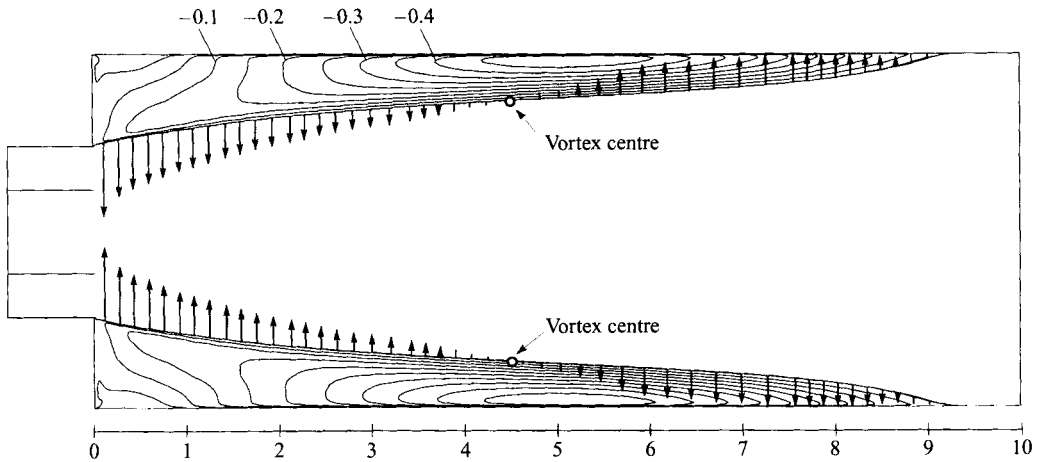
−0.1   −0.2   −0.3   −0.4

Vortex centre

Vortex centre

0   1   2   3   4   5   6   7   8   9   10

FIGURE 10. Contour plot of the negative part of the mean axial velocity component. Contour levels shown between −0.5 and 0 at intervals of 0.05. The vectors along the line of zero axial velocity represent the relative magnitude (and direction) of the mean radial velocity component along this line.

seems that only a small part of this fluid is entrained into the adjacent shear layer along the way. Most of the fuel-rich fluid came close to the base of the burner before being entrained into the step shear layer.

The vertical vectors shown along the zero axial velocity line represent the relative magnitude and direction of the mean radial velocity along this line. It is seen that the fluid inside the recirculation zone, moving towards the base of the burner, experiences increased momentum toward the centreline as it gets closer to the base of the burner.
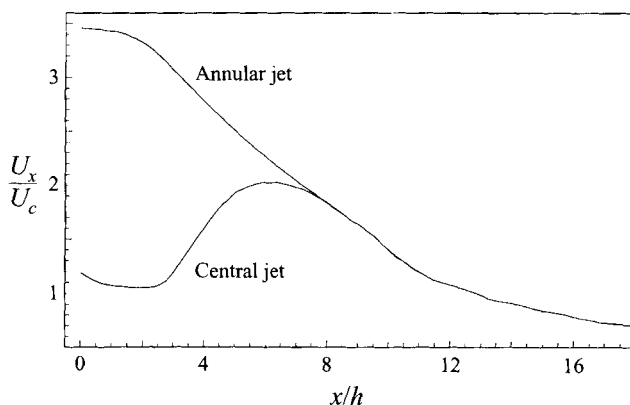
FIGURE 11. Values of the two peaks in the velocity profiles downstream of the step (caused by expansion of the central and annular jets).

In fact, the largest (negative) radial velocity along the zero axial velocity line occurs close to the base of the burner. Entrainment of (fuel-rich) fluid from the recirculation zone into the step shear layer can therefore be expected to be largest at this point. (This was also confirmed by the animated results.)

Figure 9(b) shows a contour map of the mean radial velocity component. Notice that a negative value means that U_r is directed towards the centreline. It is evident that fluid from the annular pipe is moving towards the centreline for the first 5–6 step heights following the expansion. Further downstream the radial velocity is positive indicating that fluid is moving towards the wall of the combustion chamber. Fluid from the recirculation zone is moving towards the centreline upstream of about $x/h = 4$–5. This fluid is being entrained into the step shear layer. Also notice the small region of positive U_r in the outer corner of the step. This clearly shows the existence of a secondary, counter-rotating vortex.

The point where both the axial and radial velocity components are zero (termed the 'vortex centre') is indicated by an open circle in figure 10. The vortex centre is seen to be located at about $x/h = 4.5$. Based on the magnitude of the radial velocity vectors it seems that the largest entrainment of fluid into the recirculation zone occurs roughly from about $x/h = 6$ to $x/h = 9$. This was in fact observed to be the case also in the animation. No fuel-rich fluid was seen to cross the annular stream upstream of the vortex centre. Even though isolated pockets of fuel-rich fluid were able to cross around the vortex centre, the largest entrainment of fuel into the recirculation zone seemed to occur around the instantaneous reattachment point.

Figure 11 shows the evolution of the two local peaks (resulting from expansion of the two jets) in the mean velocity profile downstream of the expansion. (The peak resulting from the central jet is just the centreline velocity.) The centreline velocity is seen to slow down slightly after expansion, up to about $x/h = 2$-2.5. Then a sharp increase is observed, indicating a significant entrainment of fluid from the annular stream. This is consistent with figure 9(b) which shows that the mean radial velocity is negative in the region from about $x/h = 2$ to $x/h = 6$. This region is clearly characterized by strong mixing. The reason for the strong mixing is likely that the shear layers from the central pipe and step intersect at about $x/h = 2$ which is accompanied by merging of vortices shed from the corner of the step (step shear layer) and the central pipe (central-pipe shear layer).

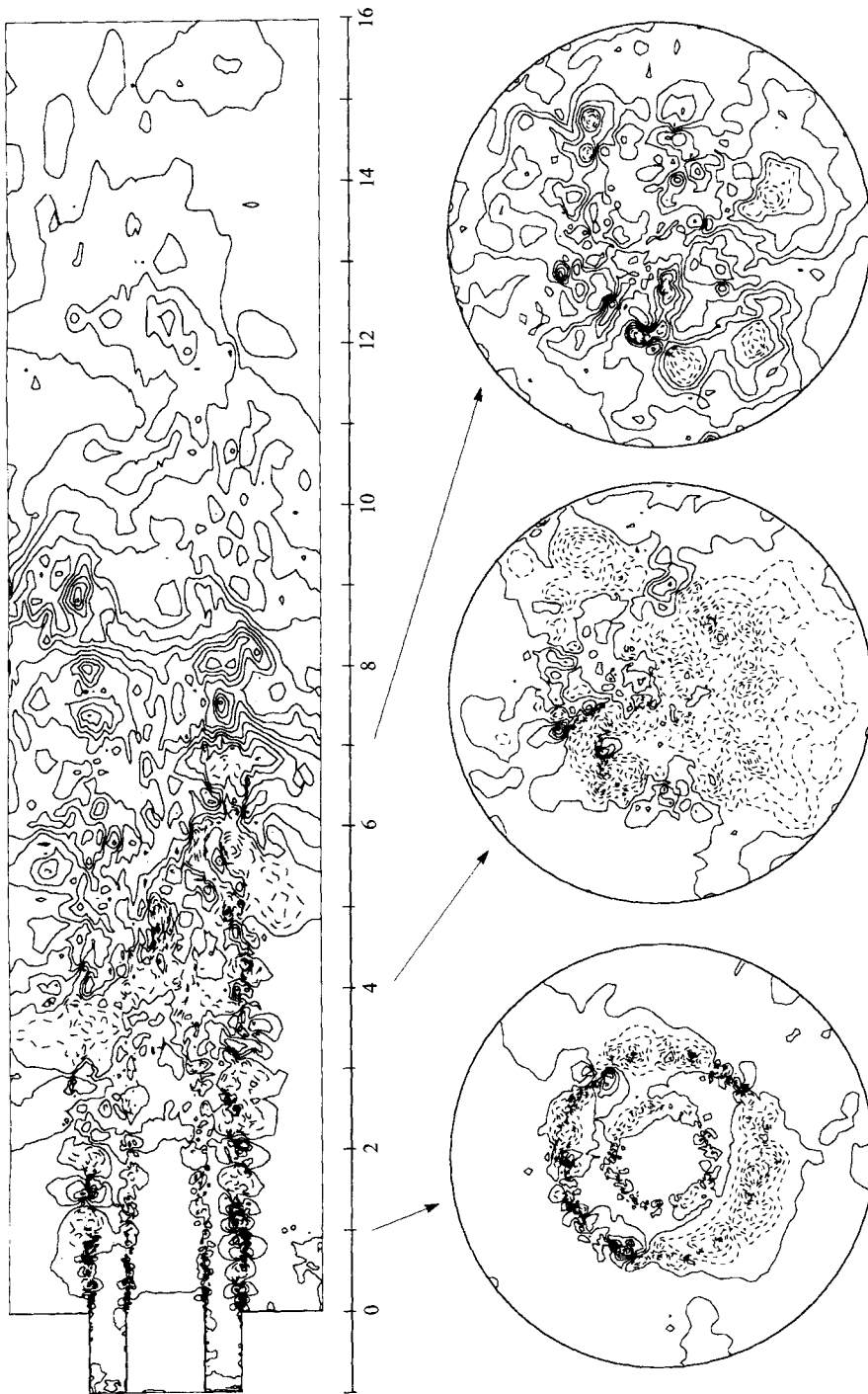The peak velocity of the annular jet is seen to decrease following the expansion

FIGURE 12. Contour plot of an instantaneous pressure field. Dashed lines denote negative values, solid lines denote positive values. Contour levels shown between −1.0 and 1.6 at intervals of 0.13.
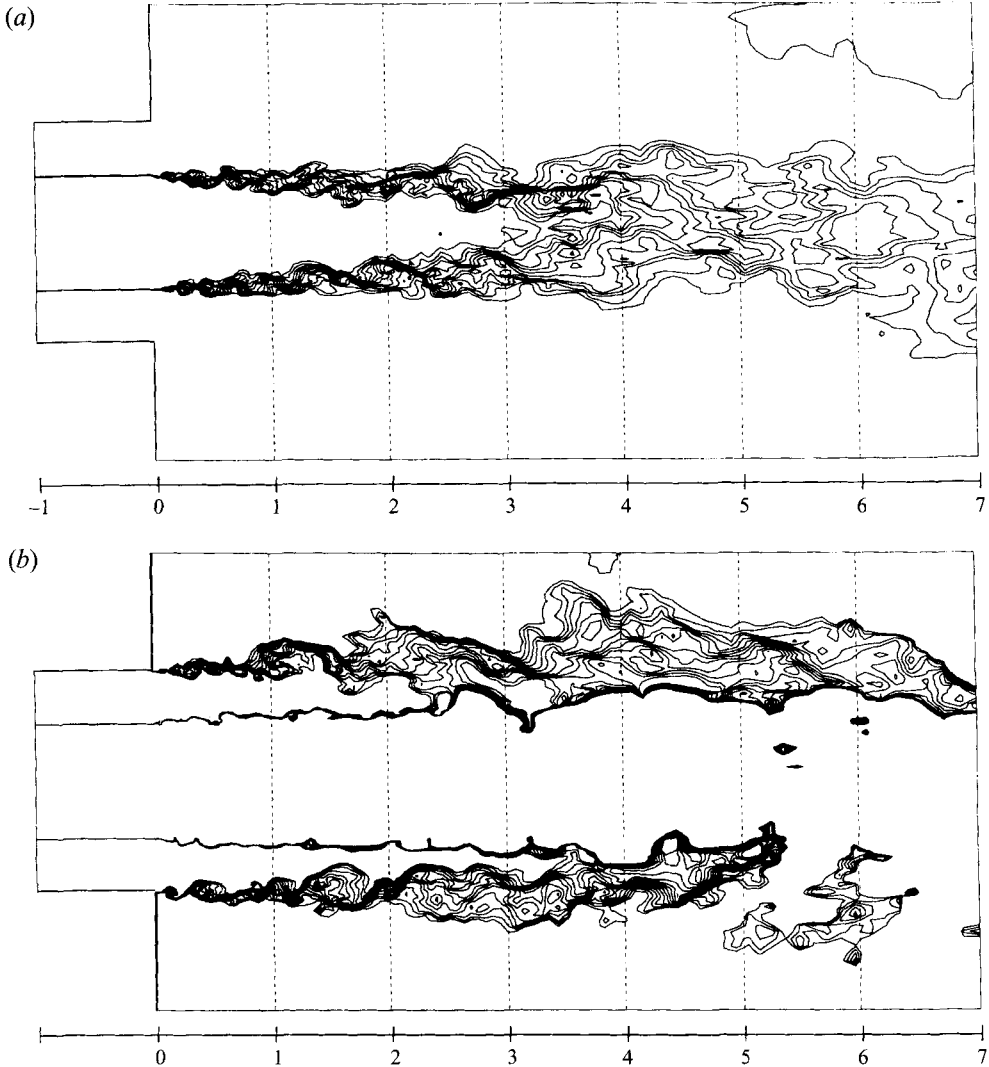
(a)

(b)

FIGURE 13. Visualization of the shear layer: contours of instantaneous fuel mass-fraction. (a) Between the central and annular jets; contour levels: 0.06 to 0.94 at steps of 0.08. (b) Between the annular jet and the recirculation zone; contour levels: 0.005 to 0.031 at steps of 0.002.

indicating a spreading of the jet throughout the combustion chamber. However, the rate of spreading is slow during the first two step heights and then increases sharply as the two shear layers intersect, thus significantly enhancing the mixing. Downstream of about $x/h = 7$ the two jets seem to be completely mixed with the peak value of the velocity profile being the centreline velocity.

5.2.2. Flow structures

Figure 12 shows an instantaneous snapshot of the pressure field in one (x, r)-plane and three cross-sections $(r, \theta$-planes). Downstream of the expansion, up to about $x/h = 2$, the figure reveals organized structures being shed, both from the corner of the step and from the end of the central pipe. The structures are seen to grow in size with increasing axial distance. Between $x/h = 2$ and $x/h = 3$ the structures from the
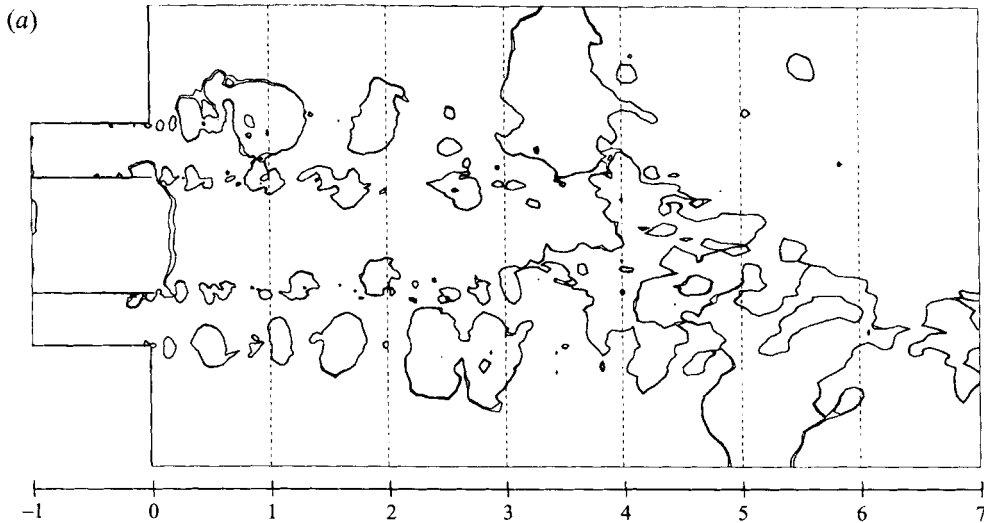
(a)

FIGURE 14. Visualization of the shear layer between the annular jet and the recirculation zone. Contours of instantaneous pressure. Contour levels: -0.074 to -0.05 at steps of 0.006.
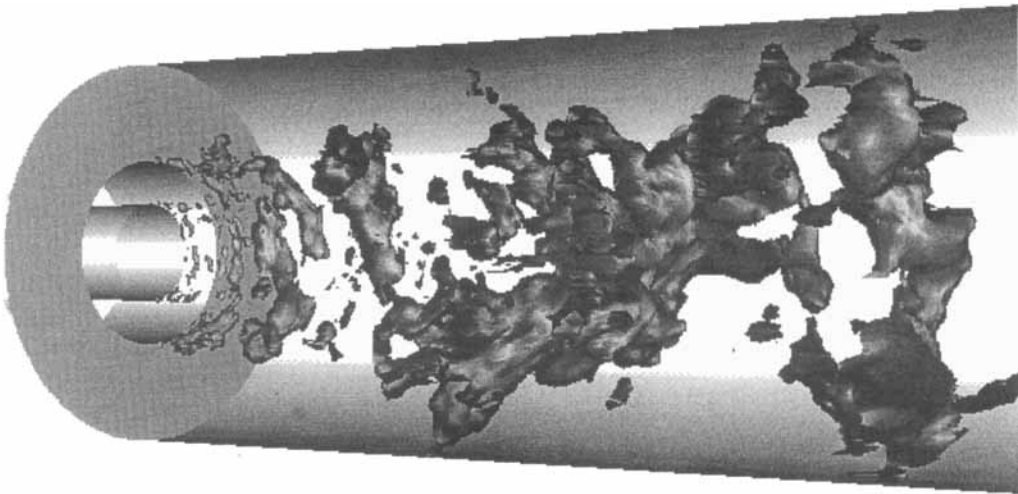

FIGURE 15. Vortical structures shed from the base of the burner, visualized using isosurfaces of instantaneous pressure fluctuations. (The plot was generated by subtracting the mean pressure from an instantaneous pressure field.)

two shear layers merge, and downstream of about $x/h = 3$–4 the clearly identifiable organized structures have all but disappeared.

To better visualize the shear layers, figures 13(a) and 13(b) focus on the first 7 step heights of the combustion chamber. The figures show instantaneous contours of the passive scalar in a band chosen to highlight the central-pipe shear layer in figure 13(a) and the step shear layer in figure 13(b). Figure 14 visualizes the shear layers using the contours of instantaneous pressure in an (x, r)-plane. A narrow interval of contour values has been chosen which is useful for identifying individual structures. Each of the enclosed surfaces represent vortical structures.

An interesting feature of figure 13 is that it clearly shows the characteristic roll-up
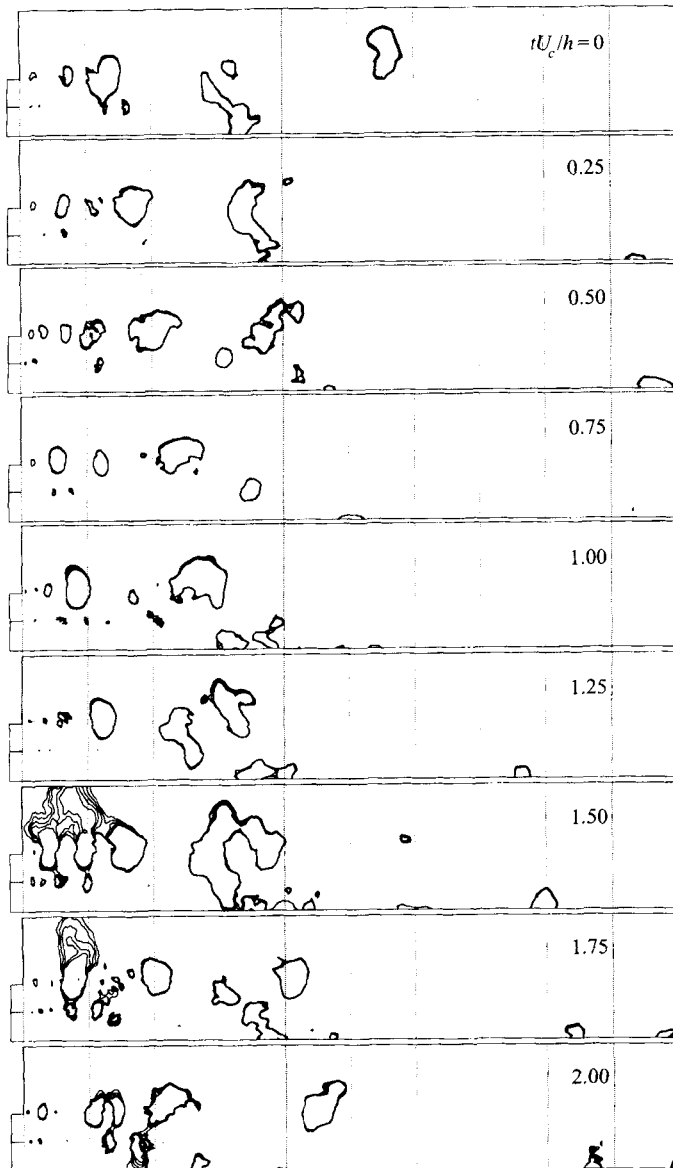
FIGURE 16. Contours of instantaneous pressure fluctuations, averaged in the azimuthal direction. The radial direction spans from $r = 0$ to $r = r_0$. Contour levels: -0.06 to -0.04 at steps of 0.004.

of vortices in the early part of the central-pipe shear layer. The rollers can be seen to correspond to the structures traced by the pressure contours in figure 14. Figure 13(a) indicates that the 'potential core' of the central jet has disappeared about 3 step heights downstream of the expansion. At this point the vortices shed from the central pipe have grown to enclose the centreline of the flow. This is consistent with figure 12 which showed the disappearance of coherent structures downstream of about $x/h = 3$. Figure 13(b) indicates that the shear layers originating from the step and from the central pipe merge between $x/h = 2$ and $x/h = 3$.

Figure 15 shows a three-dimensional view of the instantaneous pressure fluctuations. The structures are shown only for half of the azimuthal span ($\theta = 0$–$180°$). Figures
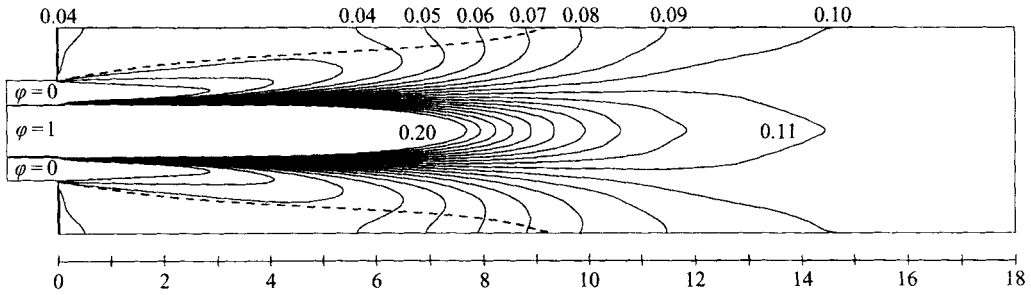
FIGURE 17. Contour lines of the mean fuel mass-fraction. The contour values range from $\varphi = 0.01$ to $\varphi = 0.2$ in steps of $\Delta\varphi = 0.01$. The concentration level is higher (up to a maximum of 1) in the core of the flow, immediately downstream of the step. The dashed lines represent the mean streamline separating the flow in the recirculation zone from that in the core.

14 and 15 show individual ring-type vortical structures being shed, both from the step and from the central pipe. The structures are seen to grow with increasing axial distance, caused by pairing of individual vortices. Between $x/h = 2$ and $x/h = 3$ the somewhat organized structures seen upstream have more or less disappeared, indicating a merging of vortices from the two shear layers. The axial convection velocity of the individual vortices is a strong function of the azimuthal position. The vortex rings therefore undergo axial stretching which rapidly breaks azimuthal coherence.

The convection of vortical structures downstream is most easily seen in figure 16, which shows a time sequence of contours of instantaneous azimuthally averaged pressure fluctuations. The plot was generated by subtracting the mean pressure from instantaneous pressure fields. This serves to identify any large-scale structure that is reasonably coherent in the azimuthal direction. (Note that each figure only shows half of the domain, i.e. from the centreline to the outer wall.) Figure 16 shows that there are indeed large-scale structures convected downstream in the combustion chamber. However, the structures tend not to be very coherent. None of the structures in figure 16 seem to survive past about $x/h = 4$. The convection velocity of the large-scale vortical structures is estimated to be about $1.6U_c$. Based on an analysis of the animated database it is further estimated that the ratio of the wavelengths of the structures in the inner and outer shear layers is about 0.3–0.5.

5.2.3. Mass transport

Figure 17 shows a contour plot of the mean mass-fraction of fuel in the combustion chamber. Contour values are plotted in the range $\varphi = 0.01$–0.20. (Higher fuel mass-fraction exists only in the core region of the flow, downstream of the central pipe.) It is seen that downstream of about $x/h = 14$ the two jets appear to be completely mixed. After complete mixing has taken place the fuel mass-fraction should be uniform and equal to the fuel mass-fraction of the fluid entering the combustor, which in the present case is 0.105. Figure 17 shows that the fuel mass-fraction near the exit of the combustor is in the range 0.10 to 0.11.

The mean reattachment point was found to be at $X_R/h = 9.4$. Figure 17 reveals that the fuel mass-fraction decreases from about 0.07 at the reattachment point to a minimum of about 0.035–0.04 when approaching the base of the burner through the recirculation zone. A slight increase in the fuel mass-fraction is found in the outer corner of the combustor, immediately downstream of the expansion point. This
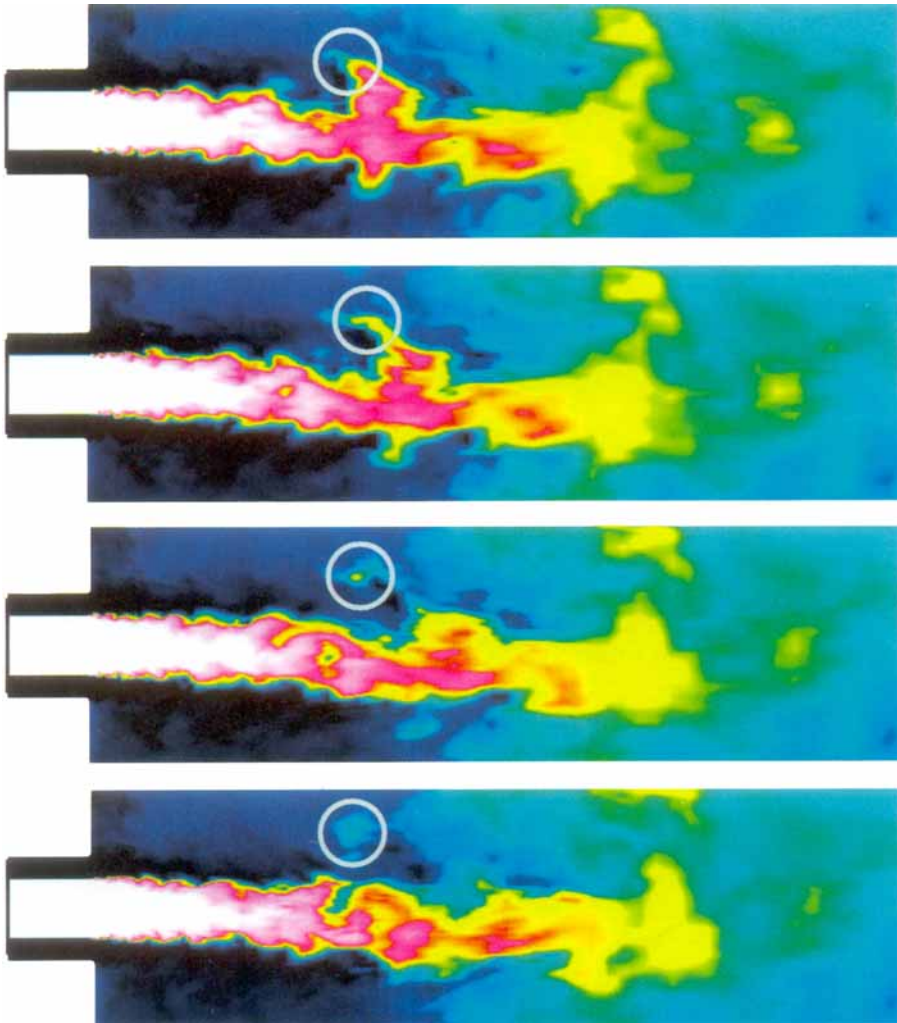
FIGURE 18. Sequence of four consecutive frames from the animation (top to bottom) showing contour levels of the fuel mass-fraction in the combustion chamber. The red circle indicates a pocket of high fuel concentration fluid escaping thorough the annular stream to be entrained in the recirculation zone. The event is taking place about $4.5h$ downstream of the expansion. The spacing between the frames is $\Delta T = 0.4h/U_c$.

region coincides with the location of a secondary, counter-rotating vortex described earlier.

The evolution of the fuel mass-fraction was animated over a period covering more than 5 flow-through times. (A flow-through time is defined to be 30 non-dimensional time-units, corresponding roughly to the time it takes a fluid particle to travel through the combustion chamber at $U_0=0.6$.) An analysis of the animation sequence indicates that most of the fuel is not able to penetrate the annular stream and is carried all the way to the reattachment point (which instantaneously varies between $x/h = 7$ and $x/h = 11$) before being entrained into the recirculation zone. This process seems to take place when large pockets of fuel hit the wall and are split, with a part moving upstream, into the recirculation zone, and a part continuing downstream. However,
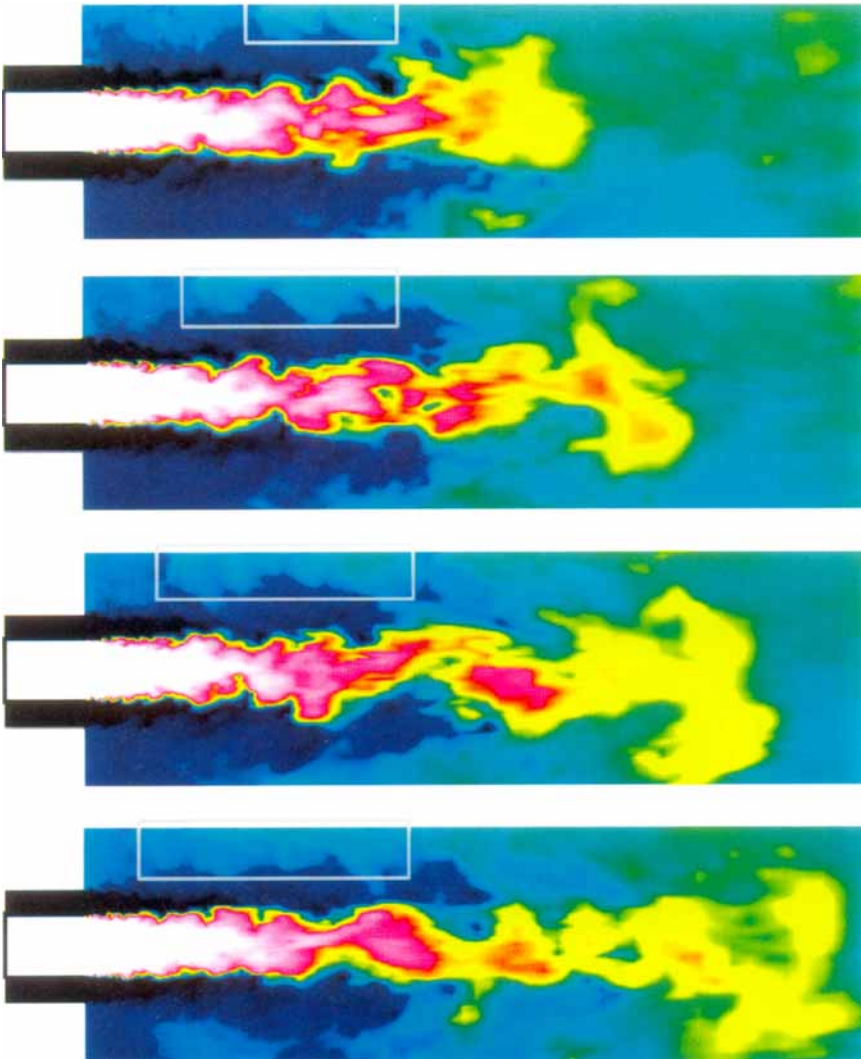
FIGURE 19. Sequence of four consecutive frames from the animation (top to bottom) showing contour levels of the fuel mass-fraction in the combustion chamber. High fuel concentration fluid is seen to move backwards toward the base of the burner in a 'belt' close to the wall. The rectangular boxes highlight this effect. The spacing between the frames is $\Delta T = 1.8h/U_c$.

intermittent pockets of fuel are able to escape through the annular stream and reach the recirculation zone as far upstream as $x/h = 4$–5 (coinciding with the location of the vortex centre), although only a small portion (of the order of a few percent) of the fuel in the recirculation zone reaches the zone by this mechanism. Figure 18 shows four frames from the animation in which a small pocket of fuel is seen to penetrate the annular jet to reach the recirculation zone before being significantly diluted. This event is taking place about 4–5h downstream of the expansion. A study of the animation further reveals that the azimuthal extent of the escaping fuel pockets is on average small, of the order of 5–10°. However fuel pockets with azimuthal extent up to 30–40° were occasionally observed.
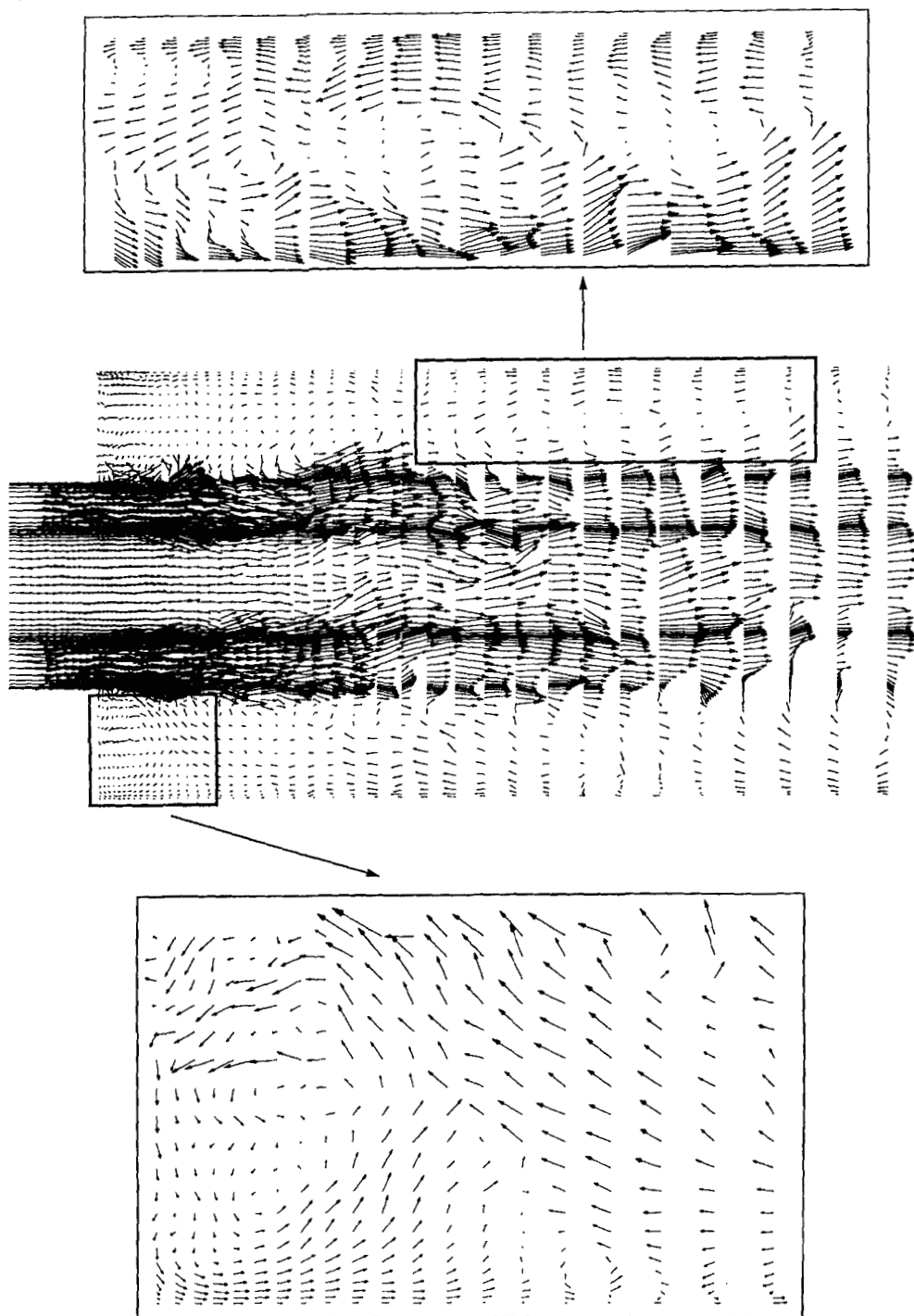
FIGURE 20. Instantaneous velocity vectors in one (x, r)-plane.

Another interesting point revealed by the animation is that pockets of nearly pure air (from the annular jet) are able to penetrate the recirculation zone at intermittent time periods, thus temporarily diluting the concentration of fuel in this region.

The fact that fuel is able to escape through the annular stream, into the recirculation zone, supports a hypothesis by Roquemore *et al.* (1991). They speculated that unburned fuel and hot combustion products escape through 'holes' in the flame to be entrained into the recirculation zone. (Holes in the flame are most likely formed in the braid regions of vortex trains where stretching and fast mixing occur.) The present calculations verify that in the absence of chemical reactions, fuel-rich pockets of fluid are indeed able to cross the annular jet without being significantly diluted. However, when adding chemical reactions, the fuel also has to avoid being consumed in the flame, a phenomenon which cannot be addressed in the present cold-flow calculations.

The animation further indicates that the fuel mass-fraction inside the recirculation zone is highest close to the wall where fluid seems to be traveling rapidly backwards toward the base of the combustion chamber. Some of the fuel-rich mixture is being entrained into the annular stream along the way, but most seems to be carried all the way back to the base of the burner. This is illustrated in figure 19 which shows four consecutive frames from the animation of the fuel mass-fraction.

This observation is supported by the findings from §5.2.1 where it was established that the maximum mean reversed axial velocity was found very close to the wall. Section 5.2.1 also showed that the radial velocity along the zero axial velocity line increased from the vortex centre towards the base of the burner, and in fact reached its peak close to the corner of the step (see figure 10). Thus, entrainment of fluid from the recirculation zone into the step shear layer is likely to be largest near the base of the burner.

During the time period covered by the animation, the concentration of fuel in the recirculation zone was highest in the region $0 < x/h < 1$, i.e. close to the base of the burner. This is likely due to the secondary, counter-rotating, vortex in the corner of the step trapping fuel-rich fluid. The counter-rotating vortex can be observed in figure 20 which shows an instantaneous vector plot of the velocity components in one (x, r)-plane. The figure shows that the backward flowing fluid from the recirculation zone is moving over the corner vortex and gets entrained in the annular jet near the tip of the step. Figure 20 further illustrates the point discussed above that there is a region of fairly large reversed flow close to the wall in the recirculation zone.

6. Conclusions

It should be stressed that the present calculations did not account for the effects of chemical reactions and heat release. The results from the above analysis therefore provide only an indication of the behaviour of the flow in the presence of a flame. However, since LBO is strongly related to the mixing and entrainment characteristics of the jets and the recirculation zone, the calculations represent a necessary first step in the analysis of LBO. The present calculation is the first fully time-dependent simulation of the mixing process taking place in a coaxial jet-combustor geometry.

Comparisons of mean quantities with corresponding experimental results of Johnson & Bennett show overall good agreement in almost all quantities. Some discrepancies do exist, but they are most likely due to problems with matching the inflow condition used in the experiment. The calculations accurately predict the fuel mass-fraction in the combustion chamber. A scalar transport version of the DM model

was used to account for subgrid-scale mass transport, and the calculations provide credence to this model.

The mean radial velocity distribution in the combustion chamber suggests that the largest entrainment of fluid into the recirculation zone takes place close to the reattachment point, which was found to be located 9.4 step heights downstream of the expansion. This finding is supported by the animated results. However, there is also intermittent transport of pockets of fuel into the recirculation zone from about 4 step heights downstream of the expansion. These pockets traverse the annular stream without being significantly diluted before reaching the recirculation zone. This result supports the notion that pockets of unburnt fuel can escape through the flame to be entrained into the recirculation zone. No fuel-rich pockets were seen traversing the annular air stream upstream of about $x/h = 4$. This location coincides roughly with the vortex centre in the recirculation zone, located at $x/h = 4.5$.

The mean axial back flow in the recirculation zone is found to be highest close to the wall. The animation shows that most of the fuel-rich fluid is transported almost to the base of the burner before being entrained into the step shear layer. This finding is consistent with the mean radial velocity distribution which shows that the radial velocity (along the zero axial velocity line) has its maximum very close to the base of the burner.

Both animated and mean results indicate that the fuel mass-fraction in the recirculation zone is highest in a small region around the outer corner of the step. This coincides with the location of a small counter-rotating vortex which seems to trap fuel-rich fluid.

An examination of large-scale flow structures shows that the step and central-pipe shear layers merge about 2–3 step heights downstream of the expansion creating a zone of intense mixing. This supports the experimental results of Roquemore et al. which showed a region of intense combustion starting about 2 step heights downstream of the expansion.

REFERENCES

AKSELVOLL, K. & MOIN, P. 1995 Large eddy simulation of turbulent confined coannular jets and turbulent flow over a backward facing step. Rep. TF-63. Thermosciences Division, Dept of Mech. Engng, Stanford University.

CABOT, W. 1991 Large eddy simulations of passive and buoyant scalars with dynamic subgrid-scale models. Center for Turbulence Research, Annual Research Briefs, 1991.

GERMANO, M., PIOMELLI, U., MOIN, P. & CABOT W. 1991 A dynamic subgrid-scale eddy-viscosity model. Phys. Fluids A 3, 1760–1765.

JOHNSON, B. V. & BENNETT, J. C. 1981 Mass and momentum turbulent transport experiments with confined coaxial jets. NASA Contractor Rep. NASA, CR-165574, UTRC Rep. R81-915540-9.

JOHNSON, B. V. & BENNETT, J. C. 1984 Statistical characteristics of velocity, concentration, mass transport, and momentum transport for coaxial jet mixing in a confined duct. J. Gas Turbines and Power 106, 121–127.

LE, H. & MOIN, P. 1994 Direct numerical simulation of flow over a backward-facing step. *Rep.* TF-58. Thermosciences Division, Dept of Mech. Engng, Stanford University.

MOIN, P., SQUIRES, K., CABOT, W. & LEE, S. 1991 A dynamic subgrid-scale model for compressible turbulence and scalar transport. *Phys. Fluids* A **3**, 2746–2757.

ROQUEMORE, W. M., REDDY, V. K., HEDMAN, P. O., POST, M. E., CHEN, T. H., GOSS, L. P., TRUMP, D., VILIMPOC, V. & STURGESS, G.J. 1991 Experimental and theoretical studies in a gas-fueled research combustor. *AIAA Paper* 91-0639.

SPALART, P. R. 1987 Hybrid RKW3 + Crank-Nicolson scheme. *Internal Rep.* NASA-Ames Research Center, Moffett Field, CA.

SPALART, P. R., MOSER, R. D. & ROGERS, M. M. 1991 Spectral methods for the Navier–Stokes equations with one infinite and two periodic directions. *J. Comput. Phys.* **96**, 297–324.